remote sensing

MDPI

Article

WBIM-GAN: A Generative Adversarial Network Based Wideband Interference Mitigation Model for Synthetic Aperture Radar

Xiaoyu Xu, Weiwei Fan *, Siyao Wang and Feng Zhou

Key Laboratory of Electronic Information Countermeasure and Simulation Technology of Ministry of Education, Xidian University, Xi'an 710071, China; xuxiaoyu@xidian.edu.cn (X.X.); 21181214081@stu.xidian.edu.cn (S.W.); fzhou@mail.xidian.edu.cn (F.Z.)

* Correspondence: wwfan@xidian.edu.cn; Tel.: +86-029-88204500

Abstract: Wideband interference (WBI) can significantly reduce the image quality and interpretation accuracy of synthetic aperture radar (SAR). To eliminate the negative effects of WBI on SAR, we propose a novel end-to-end data-driven approach to mitigate WBI. Specifically, the WBI is mitigated by an explicit function called WBI mitigation–generative adversarial network (WBIM-GAN), mapping from an input WBI-corrupted echo to its properly WBI-free echo. WBIM-GAN comprises a WBI mitigation network and a target echo discriminative network. The WBI mitigation network incorporates a deep residual network to enhance the performance of WBI mitigation while addressing the issue of gradient saturation in the deeper layers. Simultaneously, the class activation mapping technique fully demonstrates that the WBI mitigation network can localize the WBI region rather than the target echo. By utilizing the PatchGAN architecture, the target echo discriminative network can capture the local texture and statistical features of target echoes, thus improving the effectiveness of WBI mitigation. Before applying the WBIM-GAN, the short-time Fourier transform (STFT) converts SAR echoes into a time–frequency domain (TFD) to better characterize WBI features. Finally, by comparing different WBI mitigation methods applied to several real measured SAR data collected by the Sentinel-1 system, the efficiency and superiority of WBIM-GAN are proved sufficiently.

Keywords: wideband interference (WBI); WBI mitigation; synthetic aperture radar (SAR); generative adversarial network (GAN)

Citation: Xu, X.; Fan, W.; Wang, S.; Zhou, F. WBIM-GAN: A Generative Adversarial Network Based Wideband Interference Mitigation Model for Synthetic Aperture Radar. *Remote Sens.* **2024**, *16*, 910. https://doi.org/10.3390/rs16050910

Academic Editor: Dusan Gleich

Received: 15 January 2024
Revised: 26 February 2024
Accepted: 26 February 2024
Published: 4 March 2024

1. Introduction

Synthetic aperture radar (SAR) plays a crucial role in fields such as Earth observation, environmental monitoring, geological exploration, resource investigation, ground deformation monitoring, and target detection due to its capability of wide-swath and high-resolution imaging [1–4]. However, SAR echoes are often affected by radio frequency interference (RFI) from other electronic devices within the same frequency band [3,4]. The low-energy RFI can be mitigated because SAR imaging processing has a significant coherent signal-processing gain. However, the high-energy RFI would seriously reduce the image quality and interpretation accuracy of the SAR (e.g., SAR image classification, target detection, and recognition) [5,6]. Meanwhile, RFI would degrade the estimation accuracy of Doppler parameters such as the Doppler center and modulation rate, resulting in unfocused and blurred SAR imaging results [7].

Depending on the bandwidth of the RFI, it is generally divided into two categories: interference with a limited bandwidth, known as narrowband interference (NBI); and interference with a broader bandwidth, referred to as wideband interference (WBI). Compared with NBI, WBI has a larger bandwidth. As a result, the SAR image quality corrupted by WBI is worse, and the SAR image interpretation accuracy is lower. Figure 1a,c show two WBI corrupted range-time/azimuth-time domain SAR data recorded by the sentinel-1A

satellite, which uses Terrain Observation by Progressive Scans Mode (TopSAR). The red vertical lines surrounded by white ellipses in Figure 1 represent WBI. Figure 1b,d represent the corresponding two WBI-corrupted SAR data in the range–frequency azimuth-time domain. From Figure 1, it can be seen that the WBI has vital energy and high time-varying properties concerning the target echoes. Figure 2 depicts the SAR imaging results without the WBI mitigation method. It can be seen that the presence of WBI seriously obscures the information about the target in the scene, which brings significant challenges to SAR image segmentation, target detection, target identification, and other image interpretation tasks. Therefore, it is imperative to present a viable WBI mitigation algorithm to eliminate the effect caused by RFI on SAR images.

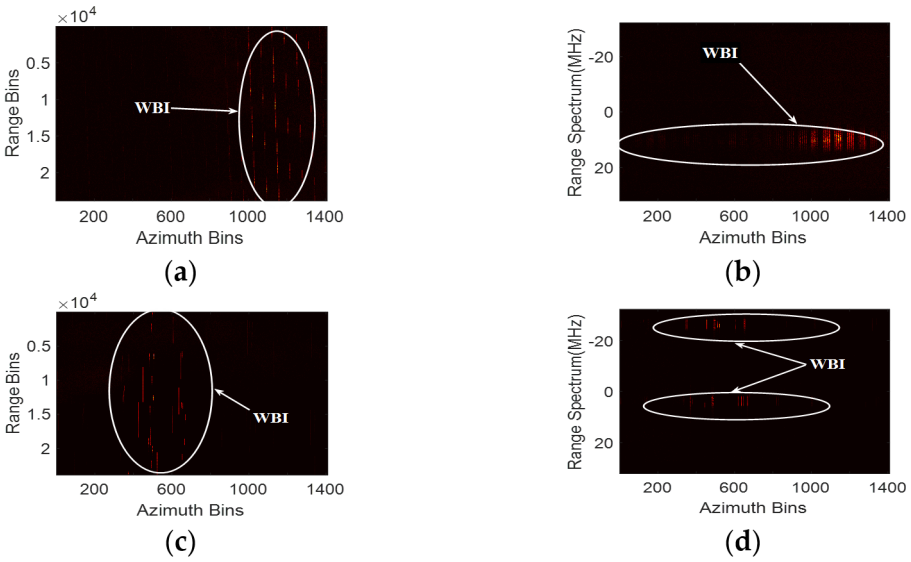

Figure 1. The real measured SAR data corrupted with WBI recorded by Sentinel-1 in (**a**,**c**) range-time/azimuth-time domain and (**b**,**d**) range–frequency azimuth-time domain.

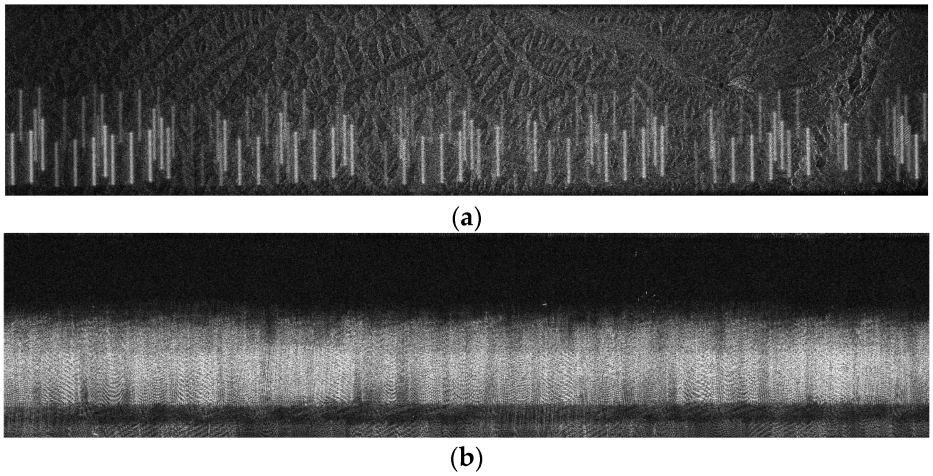

Figure 2. WBI-contaminated Sentinel-1 SAR images, which was collected of (**a**) western China on 25 August 2017 and (**b**) northeastern Germany on 8 May 2019.

1.1. Related Work

In order to reduce the influence of WBI on SAR image interpretation accuracy and imaging quality, various WBI mitigation methods have been proposed for SAR. Generally, due to the specific interference mitigation mechanisms, these methods can be divided into two groups: those that are driven by model and those that are driven by data. Model-driven methods mainly utilize physical and prior knowledge to construct parameterized

and non-parameterized WBI mitigation models and then achieve effective WBI mitigation. The parameterized WBI mitigation methods require the optimization of model parameters under specific criteria, in which SAR echoes can be expressed mathematically [8,9]. According to the assumption of the joint low rank and sparse model, various robust principal component analysis-based WBI mitigation and target echo reconstruction methods have been proposed [10–13]. Huang proposed an NBI mitigation method based on matrix-factorization decomposition, and it is also applied in WBI mitigation in SAR data and image domain [14,15]. Meanwhile, Huang proposed a proficient method for reducing WBI through an alternating projections approach, which exhibits excellent performance and rapid convergence in the two-dimensional frequency domain [16]. However, the parametric WBI mitigation methods require high model accuracy, and the model's error would severely hinder the effectiveness of WBI mitigation. The nonparametric methods for mitigating WBI primarily generate effective filters in a specific feature domain to remove the WBI and recover useful target signals. Tao proposed a WBI mitigation method for SAR, which initially converts the SAR echo corrupted with WBI into the time–frequency domain (TFD), using the STFT [13]. Then, the original problem of WBI mitigation of the range spectrum will be reduced to the problem of NBI mitigation of a series of instantaneous spectrums. However, the implementation of this method comes at the cost of high computational complexity. Yang proposed a method using an iterative adaptive approach and the orthogonal subspace projection method. It improves the instantaneous frequency resolution in STFT, using the IAA method, and filters the WBI based on the OSP method [17]. However, this method requires that the WBI is not overlapped with the useful target echo, and its computation complexity is very high.

The WBI mitigation techniques are data-driven and primarily make use of extensive SAR data that are contaminated with WBI. These data are then employed to train a WBI mitigation network, using deep learning algorithms. As is well known, deep learning is widely used in image classification [18], target detection [19], image semantic segmentation [20], image denoising [21], image super-resolution [22], image generation [23–25], image transformation [26], and RFI mitigation [27,28] because of its ability to obtain the targets' hierarchical characteristics in images automatically. The data-driven WBI mitigation techniques can adaptively capture complex characteristics of WBI in various domains. These methods efficiently use a high-throughput parameter space to map the WBI and the target signal. Fan proposed a WBI mitigation algorithm that is implemented by utilizing deep residual networks (IMNs), which can effectively eliminate NBI and WBI for SAR [29]. Nair developed a technique for mitigating RFI by using the UNet framework, which can enhance the quality of raw UWB radar data by suppressing undesired signals [30]. Fuchs suggested a convolutional neural network with complex values to alleviate the RFI; however, it might lead to signal loss in the suppression scenarios of SAR WBI [31]. Zhang proposed a novel method for SAR image interference suppression, which is implemented by constructing a coding–decoding network [32]. Wei introduced an effective technique for suppressing interference in SAR images by using the Combined-Attention Restoration Network [33]. Refs. [32,33] effectively suppressed RFI, but their methods may have caused some scene information to be lost from the RFI mitigation results shown in the articles. In short, data-driven methods have received more and more attention due to their ability to use deep learning to reconstruct the useful target signal adaptively in multidimensional domains without relying on professional knowledge. However, there is much room for improving the performance of the data-driven-based WBI mitigation network. For example, there are obvious statistical disparities between the WBI and the relevant target signal in the time–frequency spectrogram. Simultaneously, the WBI has sparse and specific structural characteristics in the time–frequency spectrogram. However, IMN only utilizes the amplitude features of WBI in the time–frequency spectrum, while the structural and statistical characteristics of WBI are not fully utilized.

This paper presents a novel method to mitigate the WBI that is implemented by employing generative adversarial networks (WBIM-GANs) for SAR. It combines the ca-

pabilities of GAN in feature intelligence extraction and the strong data-fitting ability to fully capture the statistical and structural characteristics of the WBI in the time–frequency spectrogram. Firstly, the SAR echo signal corrupted with WBI is expressed in the time–frequency domain by using a short-time Fourier transform (STFT), which could more easily depict the distinctiveness between the WBI and the target signal. Secondly, the GAN combined with the PatchGAN structure is adapted to mitigate WBI, whose aim is to learn an explicit function mapping from a WBI-corrupted SAR echo to a WBI-free SAR echo. It can improve the WBI feature extraction accuracy and reconstruct useful target signals with lower loss. Finally, the SAR echo signal, which has been restored without WBI, is converted into the time domain through the implementation of the inverse short-time Fourier transform (ISTFT). It is essential to acknowledge that the SAR echo appears as a complex signal in the time–frequency spectrogram. To effectively preserve the phase information of the SAR echo, the input of the WBIM-GAN consists of a real part of the SAR echo channel and an imaginary part of the SAR echo channel. Simultaneously, WBIM-GAN can be implemented in parallel along the azimuth dimensions, leading to a further decrease in computation time.

1.2. Main Contributions

This paper is an extension of [27]. The primary advancements of the WBIM-GAN introduced in this paper can be outlined as follows:

1. A novel algorithm for mitigating WBI by using GAN is introduced, which can achieve WBI feature fast extraction and useful target signal accuracy reconstruction with less loss. In contrast to the conventional WBI mitigation algorithm utilized for SAR, the WBIM-GAN learns an explicit function mapping from the WBI-corrupted SAR echo to the WBI-free SAR echo in an end-to-end data-driven way. It simplifies the difficulty of designing the WBI mitigation algorithm because it does not require prior knowledge.
2. The WBIM-GAN, which is integrated with the PatchGAN architecture, is capable of capturing the statistical and structural characteristics of the WBI effectively. Meanwhile, it can improve the accuracy of WBI feature extraction and reduce the loss of recovered useful target signals.
3. The effectiveness, validity, and generalization of the WBIM-GAN was confirmed on multiple measure SAR data in TopSAR mode. At the same time, the class activation mapping techniques fully demonstrate that the WBIM-GAN is more concerned with the WBI feature, which further proves its effectiveness.

The remainder of this article is arranged as follows. Section 2 presents the WBI formulation, WBI detection method, and WBI mitigation algorithm using GAN. Section 3 explains the experiment's results in detail and demonstrates the WBIM-GAN's performance on several measured SAR data. Finally, the discussion and conclusion of this paper are given in Sections 4 and 5. Additionally, there are some abbreviations to simplify the academic terminology, and these are listed in Table 1.

Table 1. Comparison table of abbreviations.

Abbr.	Full Name	Abbr.	Full Name
WBI	Wideband interference	IMN	Interference mitigation network
SAR	Synthetic aperture radar	ISTFT	Inverse short-time Fourier transform
WBIM-GAN	WBI mitigation–generative adversarial network	Conv	Convolutional layers
STFT	Short-time Fourier transform	ReLU	Linear unit layers
TFD	Time–frequency domain	BN	Batch normalization layer

Table 1. *Cont.*

Abbr.	Full Name	Abbr.	Full Name
GAN	Generative adversarial network	Es	Elementwise sum layer
RFI	Radio frequency interference	SDR	Signal-distortion ratio
NBI	Narrowband interference	MNR	Multiplicative noise ratio
PRF	Pulse repetition frequency	SSIM	Structure similarity
TopSAR	Terrain Observation by Progressive Scans Mode	PSNR	Peak signal-to-noise ratio
RMSE	Root mean square error	JSR	Jam-to-signal ratios
ISNF	Instantaneous-spectrum notch filtering	ESP	Eigenspace projection
MFD	Matrix factorization decomposition	IAA	Iterative adaptive approach

2. WBI Expressions and Methodology

In this section, various mathematical formulas are employed to interpret the WBI, and the characteristics of WBI in the multidimensional domain are analyzed. Then, a WBI detection method based on kurtosis in the TFD is presented. Meanwhile, the WBI mitigation method based on GAN (WBIM-GAN) and the detailed network structure are introduced. Moreover, some quantitative parameters are used to measure the effectiveness of the proposed method.

2.1. WBI Formulation

The SAR can be expressed as the following formulation, with the range time set to t and the azimuth time set to τ:

$$x(t,\tau) = s(t,\tau) + j(t,\tau) + n(t,\tau) \tag{1}$$

where $s(t,\tau)$ denotes the valuable target signal, $j(t,\tau)$ denotes the WBI, and $n(t,\tau)$ denotes the additional noise. Generally, the WBI can be divided into two forms: chirp-modulated WBI and sinusoidal-modulated WBI. The WBI with chirp modulation can be modeled as

$$I_{CM}(t,\tau) = \sum_{k=1}^{K} a_k(t,\tau) \exp\left\{ j\left(2\pi f_k t + \pi \gamma_k t^2\right)\right\} \tag{2}$$

where $a_k(t,\tau)$ denotes the complex envelope, f_k denotes the frequency, γ_k denotes the chirp rate, and the subscript k of these three parameters represents the kth WBI component. Meanwhile, the WBI with sinusoidal modulation is formulated as

$$I_{SM}(t,\tau) = \sum_{k=1}^{K} a_k(t,\tau) \exp\{j\beta_k \sin(2\pi f_k n + \phi_k)\} \tag{3}$$

where $a_k(t,\tau)$ represents the complex waveform, β_k represents the modulation parameter, and ϕ_k represents the original phase. And the subscript k of these three parameters represents the kth WBI component as well.

Usually, the SAR echoes are frequently interfered with by the chirp-modulated WBI. Figure 3a is the SAR echo in the range-time domain, which is the 601th pulse of the SAR data shown in Figure 1a. Meanwhile, Figure 3d is the SAR echo in the range-time domain, which is the 1069th pulse of the SAR data shown in Figure 1b. It is evident that SAR echoes are contaminated with the WBI. At the same time, WBI is time-varying, and its amplitude is significantly higher than the amplitude of the target signal. Moreover, there is a significant difference in the amplitude variation of the WBI depicted in Figure 3a,d. Figure 3b,e show the WBI in the range–frequency domain. It is obvious that the WBI possesses a greater share of frequency units within the frequency–range domain, and its amplitude is significantly stronger compared to the useful target signal. Figure 3c,f displays

the time–frequency spectrogram of WBI. It is obvious that the WBI in Figure 3c is chirp-modulated. Furthermore, the WBI exhibits significantly greater strength compared to the valuable target signal. Simultaneously, the WBI in Figure 3f is composed of multiple chirp-modulated WBIs. Meanwhile, the WBI in the TFD can characterize not only its temporal and spectral features but also its time–frequency modulation and structure characteristics, which provide the foundation for further WBI mitigation.

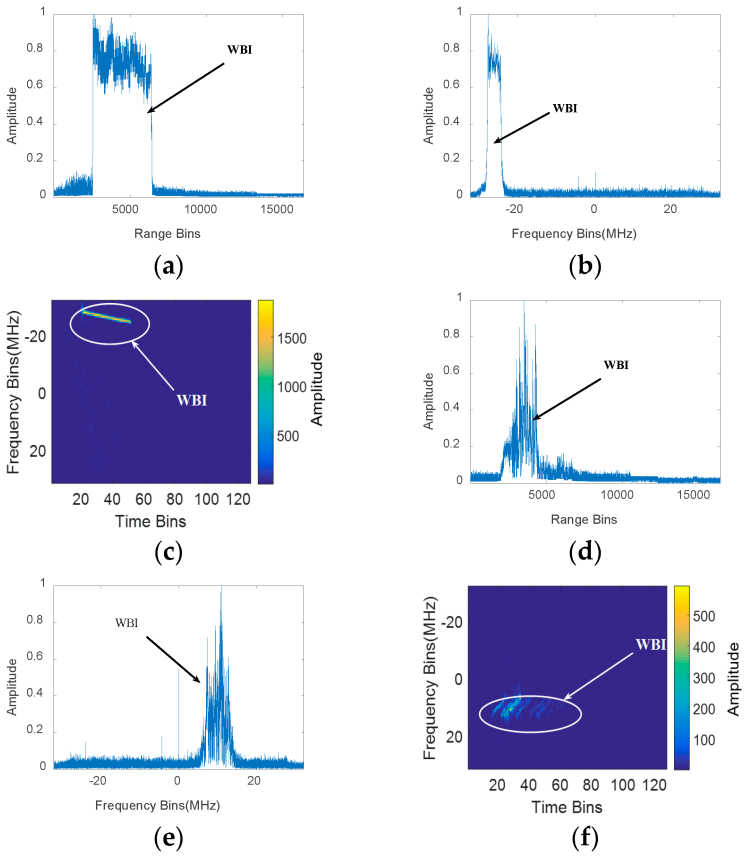

Figure 3. WBI-contaminated SAR echoes in (**a**,**b**) range time, (**d**,**e**) range–frequency, and (**c**,**f**) range TFD.

2.2. WBI Detection

Figure 1 shows that the WBI is not present in every SAR pulse. Therefore, it is necessary to determine whether there is WBI in the SAR echo. Otherwise, the WBI mitigation methods may cause useful target signal loss. Most traditional RFI detection methods are designed for NBI, and due to the energy of the NBI, the target signal is quite different. Thus, NBI can be detected. Moreover, a hard threshold based on prior information was primarily developed. However, the performance of this type of method would be seriously degraded when there are vital scattering targets in the SAR echoes. Meanwhile, this type of RFI detection algorithm relies heavily on threshold selection. If the chosen threshold is too high, it will increase the probability of missed WBI detection. If the threshold is set too low, it will inevitably increase the probability of false alarms.

To improve the applicability of threshold selection, Meyer designed a threshold adaptive selection method based on the Neyman–Pearson criterion to enhance the RFI detection precision [34]. From Figure 4a, we can see that WBI-free SAR echoes in the TFD are Gaussian distributed, while SAR echoes corrupted with WBI have non-Gaussian characteristics. Since the statistical characteristics of SAR echo are significantly different from WBI, a Gaussian distribution parameter can be used to measure their difference, thus detecting the WBI. From the knowledge of information and statistical theory, kurtosis is usually used to measure the non-Gaussian properties of data. Figure 4a shows that in the TFD, the kurtosis

of SAR echo without WBI is 5.78, while the kurtosis of SAR echo with WBI is 482.68. Zhou proposed an adaptive NBI detection method based on kurtosis [35]. Since NBI and the target signal have obvious statistical differences in TFD, the Neiman–Pearson criterion is fully used to detect NBI. However, this method is only used for NBI and is no longer suitable for WBI detection.

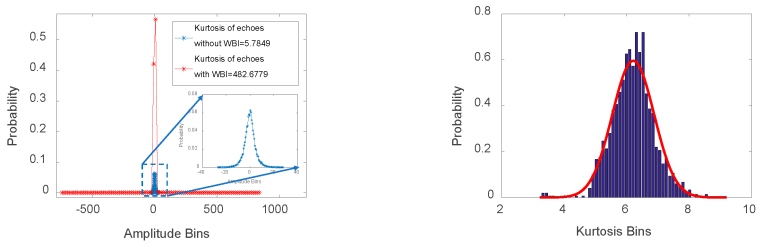

(**a**) (**b**)

Figure 4. Illustration of (**a**) statistical comparison of WBI-free instantaneous spectrum and WBI-corrupted instantaneous spectrum and (**b**) histogram of WBI-free SAR echoes' kurtosis with a distribution fit.

As shown in Figure 3, the characteristics of the WBI in the TFD are dramatically different from target signals. Therefore, the WBI detection method can also be designed in the TFD. The statistical distribution of the kurtosis of the WBI-free SAR echo in the TFD follows the Gaussian distribution depicted in Figure 4b. Meanwhile, the kurtosis of the SAR echo with WBI shown in Figure 4a is 482.68, and it should be on the heavy tail of the Gaussian distribution shown in Figure 4b. Therefore, this paper proposes a WBI detection method for SAR based on the Neyman–Pearson criterion and utilizes the kurtosis diversity of the WBI and the target signal in the TFD. Furthermore, it transforms the WBI detection into a task of binary classification, which is formulated as

$$flag = \begin{cases} 1, & k \geq \eta^* \\ 0, & k < \eta^* \end{cases} \tag{4}$$

where $flag$ denotes the WBI detection result, $flag = 1$ indicates that WBI presents in the SAR echo, $flag = 0$ indicates that there is no WBI, η^* denotes the kurtosis threshold, and k represents the kurtosis of the SAR echo in the TFD.

Therefore, the critical issue of WBI detection is finding the optimal threshold, η^*. If η^* is set too high, it will lead to missed detection of the WBI, which would degrade the SAR image quality. If the η^* is set too low, the false alarm of the WBI detection will increase, which would result in the SAR echo loss and an increase in the WBI mitigation processing time. Thus, the optimization goal of η^* will improve the WBI detection probability and ensure that the false alarm remains within the tolerable range. As a result, η^* can be expressed as the following optimization problem:

$$\begin{aligned} \eta^* &= \text{argmax} P_D \\ &subject\ to\ P_F < \alpha \end{aligned} \tag{5}$$

where the false-alarm rate, α, generally is set to 1×10^{-6}.

Furthermore, η^* can be determined by the Neyman–Person criterion and is based on the rate of false-alarm constrain, and the property of the WBI-free SAR echo's kurtosis follows Gaussian distribution, leading to

$$\alpha = \int_{\eta^*}^{\infty} \frac{1}{\sqrt{2\pi\sigma^2}} e^{\frac{-(x-\mu)^2}{2\sigma^2}} dx = \frac{1}{2}\left[1 - erf\left(\frac{\eta^* - \mu}{\sqrt{2}\sigma}\right)\right] \tag{6}$$

where μ refers to the mean, and σ refers to the standard deviation of the WBI-free SAR echo in the TFD. According to the relationship of the α and the η^*, η^* can be given by

$$\eta^* = \mu + \sqrt{2}\sigma erf^{-1}(1 - 2\alpha) \tag{7}$$

2.3. WBIM-GAN

The fundamental theory of the WBI mitigation algorithm is to identify the inherent distinctions between the WBI and the target signal. Deep learning has the ability to dynamically capture complex features from the targets in a high-dimensional space. Meanwhile, it possesses a robust capacity for nonlinear representation, allowing for the accurate approximation of intricate functions. The problem of reducing WBI in SAR can be reframed as a sophisticated process of optimizing a complex function. In this process, the given input is a SAR echo that has been corrupted with WBI in a particular domain, and the intended outcome is to obtain a restored SAR echo that is free from WBI. As a result, we introduce the WBIM-GAN in the TFD, and the purpose is to design a mapping mechanism to characterize the relationship between WBI-affected SAR echo and WBI-unaffected SAR echo.

The generative adversarial network (GAN) is an emerging generative framework that draws inspiration from the zero-sum game theory. It is composed of a generative network and a discriminative network. The generative network acquires knowledge from real-world examples and produces fabricated samples, whereas the discriminative network assesses the genuineness of the samples. Throughout the training procedure, the generator consistently enhances the authenticity of the counterfeit samples that are produced. At the same time, the discriminatory network imposes penalties on the produced samples, thereby compelling the generative network to generate samples of superior quality. In this way, the GAN can consistently diminish the statistical disparity between the generated and authentic samples. As a result, the WBIM-GAN is composed by a network G for mitigating WBI and a network D for discriminating WBI. The G is employed to reduce WBI and produce the SAR echo without WBI. At the same time, the D is employed to differentiate the accuracy of the WBI mitigated SAR echo produced by the G. The G utilizes the integration of the deep residual network to enhance the effectiveness of WBI mitigation while solving the gradient saturation problem in the deeper layers. Meanwhile, it D employs the PatchGAN framework to capture the local details and statistical characteristics of the target echoes, thereby augmenting the effectiveness of WBI mitigation.

The structure of WBIM-GAN is depicted in Figure 5. The input of the G is the real and imaginary parts of the SAR echoes corrupted with WBI. The input of the G is the real and imaginary parts of the WBI-corrupted SAR echoes in the TFD. Table 2 depicts the structure of G; it can be seen that the G is composed of 11 residual blocks, 3 convolutional layers (Conv), 3 rectified linear unit layers (ReLU), and 1 Batch normalization layer (BN). Among them, the residual block is composed of 2 Conv, 2 BN, 1 ReLu, and 1 Elementwise sum layer (Es). The size of the Conv's kernel is 3×3, the stride is 1, and the number of output feature maps is 64. The D employs the PatchGAN technology to assess the target echo reconstruction accuracy of various sections of the SAR echo in the TFD. This technology has the potential to enhance the D's effectiveness in evaluating the genuineness of the input samples. At the same time, it enables G to comprehend the structural characteristics of the WBI and produce a more polished WBI-free SAR echo in the TFD. The D employs a sequence of Conv-BN-Leaky ReLU layers to capture the intricate characteristics of the WBI in higher dimensions. Then, it proceeds to assess whether the input corresponds to a SAR echo without WBI. Table 3 finds the detailed architecture of the D.

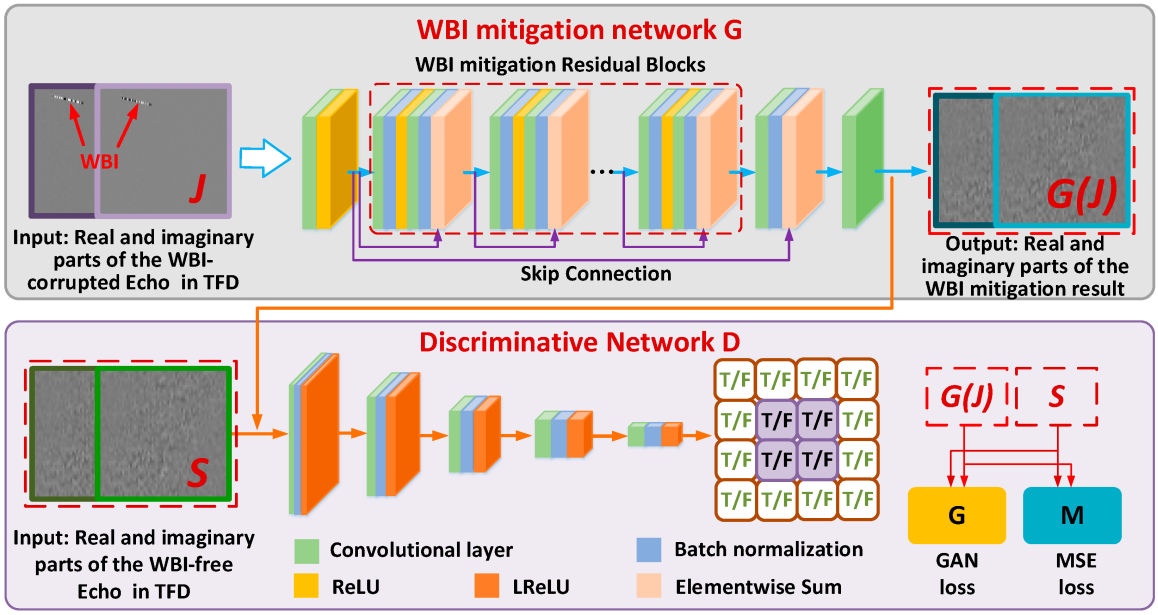

Figure 5. The structure of the designed WBIM-GAN.

Table 2. The structure of the WBI mitigation network.

Input: Complex SAR echoes contaminated with WBI in the TFD	
G-L1	[9 × 9, 64], s = 1;
G-B1	[3 × 3, 64], s = 1; BN; [3 × 3, 64], s = 1; BN; Es. (*G*-L1);
G-B2	[3 × 3, 64], s = 1; BN; [3 × 3, 64], s = 1; BN; Es. (*G*-B1);
.....	
G-B11	[3 × 3, 64], s = 1; BN; [3 × 3, 64], s = 1; BN; Es. (*G*-B10);
G-L2	[3 × 3, 64], s = 1; BN; Es. (*G*-L1);
G-Output	[3 × 3, 2], s = 1;

Table 3. The architecture of the WBI discriminative network.

Input: Generated the SAR echoes without WBI or WBI-free SAR echoes in the TFD	
D-L1	[3 × 3, 16], s = 1;
D-L2	[3 × 3, 16], s = 1; BN;
D-L3	[3 × 3, 32], s = 1; BN;
D-L4	[3 × 3, 32], s = 1; BN;
D-L5	[3 × 3, 64], s = 1; BN;
D-L6	[3 × 3, 64], s = 1; BN;
D-L7	[3 × 3, 128], s = 1; BN;
D-L8	[3 × 3, 128], s = 1; BN;
D-Output	[3 × 3, 1], s = 1;

WBIM-GAN takes advantage of the mean square error and the WGAN-GP loss function to train the network 28. The loss function of WGAN-GP can solve the problem of

vanishing and exploding gradients in WBIM-GAN training and simultaneously enhance the accuracy of the generated SAR echoes without WBI. The loss function of WBIM-GAN can be expressed as

$$\min_{G} \max_{D} L_G + \lambda_1 L_M \tag{8}$$

where L_G and L_M are the WGAN-GP loss and mean square error, respectively. And the L_G and L_M can be expressed as

$$L_G = \mathbb{E}_{S\sim p_{data}}[D(S)] - \mathbb{E}_{J\sim p_z}[D(G(J))] \quad - \lambda_2 \mathbb{E}_{\hat{X}_w \sim p_{penalty}}\left[\left(\left\|\nabla_{\hat{x}} D\left(\hat{X}_w\right)\right\| - 1\right)^2\right] \tag{9}$$

$$L_M = \mathbb{E}\left[(S - G(J))^2\right] \tag{10}$$

where S and J represent the desired target signal and the SAR echo contaminated with WBI in the TFD, respectively. Meanwhile, the $\hat{X}_w$ can be updated via the rule, $\hat{X}_w \leftarrow \varepsilon G(J) + (1-\varepsilon)S$. Moreover, λ_1 and λ_2 are regularization parameters that balance the terms in Equations (8) and (9), respectively.

The WBI-corrupted SAR echoes are transformed into TFD with the size of 128×128 complex matrices by using STFT. Meanwhile, the real and imaginary parts are normalized to [−1,1], respectively. The Pytorch 1.8.0+cu101 on the NVIDIA Titan-X Graphics Processing Unit (GPU) is utilized to train and test the WBIM-GAN. Meanwhile, the stochastic gradient descent algorithm is used to train the parameters of the WBIM-GAN. Moreover, the minimum batch size, momentum, weight decay coefficient, and learning rate (λ_1) are, respectively, set to 32, 0.9, 0.0005, and 0.0001.

2.4. Evaluation Measures

The efficacy and superiority of the WBIM-GAN were validated through qualitative examination and quantitative measures. The qualitative assessment is generally processed by visually comparing the target signal reconstructed precision in the TFD and the SAR imaging results with the implementation of various WBI mitigation methods. Meanwhile, the signal distortion ratio (SDR), multiplicative noise ratio (MNR) [21], structure similarity (SSIM), peak signal-to-noise ratio (PSNR), and root mean square error (RMSE) are utilized to quantitative assess the WBI mitigation performance. Among them, the SDR is generally used on simulated data. Meanwhile, the MNR, SSIM, PSNR, and RMSE metrics are utilized to validate the real SAR data.

The SDR is defined as the normalized energy loss of the target signal after WBI mitigation. It is usually used to estimate the distortion of the target signal after WBI mitigation, and its formulation is

$$SDR = 10\log_{10}\left(\frac{\sum|x_0 - \hat{x}|^2}{\sum|x_0|^2}\right) \tag{11}$$

where x_0 denotes the WBI-free SAR echo, and $\hat{x}$ is the reconstructed signal after WBI mitigation. The smaller the SDR value, the better the target echo reconstruction performance and the lower the distortion.

The MNR is an important interference mitigation performance assessment metric that assesses the average energy proportion between the no-return area and the neighboring bright area in SAR images. It can be expressed as

$$MNR = 10\log_{10}\left(\frac{\frac{1}{N}\sum_{n=1}^{N}|SARIP_n|^2}{\frac{1}{M}\sum_{m=1}^{M}|SARIP_m|^2}\right) \tag{12}$$

where N denotes the pixel's number of the no-return region, M denotes the pixel's number of the highlighted region, $SARIP_n$ represents the pixel values of no-return region, and

$SARIP_m$ represents the pixel values of highlighted region. The smaller the MNR value, the higher image contrast and the better the recovery performance

The SSIM is utilized to quantify the disparity between the recovered SAR image and original SAR image without WBI, and its mathematical definition is

$$\mathrm{SSIM} = \frac{(2\mu_R\mu_O + C_1)(2\sigma_{RO} + C_2)}{(\mu_R^2 + \mu_O^2 + C_1)(\sigma_R^2 + \sigma_O^2 + C_1)} \tag{13}$$

where O and R denote the initial SAR image without WBI and recovered SAR image after WBI mitigation, respectively; $\mu_{|\cdot|}$ and $\sigma^2_{|\cdot|}$ represent the mean and variance; $\sigma_{|\mathbf{x}||\mathbf{x}_0|}$ denotes the covariance; $C_1 = (0.01 \times F)^2$ and $C_2 = (0.03 \times F)^2$ are the constant factors; and F represents the range of amplitude fluctuation. It is obvious that a higher SSIM value indicates a lower information loss in the SAR image.

The PSNR serves as a WBI mitigation assessment metric to quantify the similarity between the recovered SAR image and the initial SAR image without WBI, which denotes the peak ratio of signal power to noise power. The PSNR can be presented as

$$PSNR = 10\log_{10}\left(\frac{MAX_O^2}{\frac{1}{MN}\sum_{m=1}^{M}\sum_{n=1}^{N}\|O(m,n) - R(m,n)\|^2}\right) \tag{14}$$

where MAX_I indicates the maximum value of the SAR image without WBI; and M and N are pixel num of SAR images in height and width dimensions, respectively. It can be seen that a higher PSNR indicates less SAR image loss.

The RMSE is used to assess the deviation of the recovered SAR image and from the original SAR image, and the formulation is as follows:

$$RMSE = \frac{\|O - R\|_F}{\|O\|_F} \tag{15}$$

A lower RMSE represents a better WBI mitigation performance.

3. Experimental Results

In this part, the detailed introduction of the WBI mitigation dataset is presented initially. Then, the experimental details of the proposed WBIM-GAN and the comparison algorithms performed on simulated data are demonstrated. Finally, the accuracy and effectiveness of the WBIM-GAN method are verified through comparative experiments by using real measured SAR data collected by Sentinel.

3.1. Datasets

The WBIM-GAN transforms the WBI mitigation into a problem of WBI-free SAR echo generation. Therefore, the WBIM-GAN dataset includes WBI-corrupted SAR echoes, and WBI-free SAR echoes in the TFD. The SAR echoes corrupted with WBI in the TFD are the input of WBIM-GAN, and the SAR echoes without WBI in the TFD are the label. Figure 6 shows several label samples of real measured WBI-free SAR echoes in the TFD. The real measured SAR echoes were collected by Sentinel-1, and the sample size is 128 × 128. Figure 7 shows several samples of WBI-corrupted SAR echoes in the TFD, which are obtained by adding simulated chirp-modulated WBI with different signal-to-interference ratios to the real measured SAR echoes. Meanwhile, it can be seen that there are differences in the location, modulation frequency, number, and structure of the samples, which are diverse. There are a total of 46,748 samples in the WBIM-GAN dataset. Moreover, 80% of the samples are the training set, and 20% of the samples are the validation set. The test set is the real measured WBI-corrupted SAR echoes collected by the Sentinel-1.

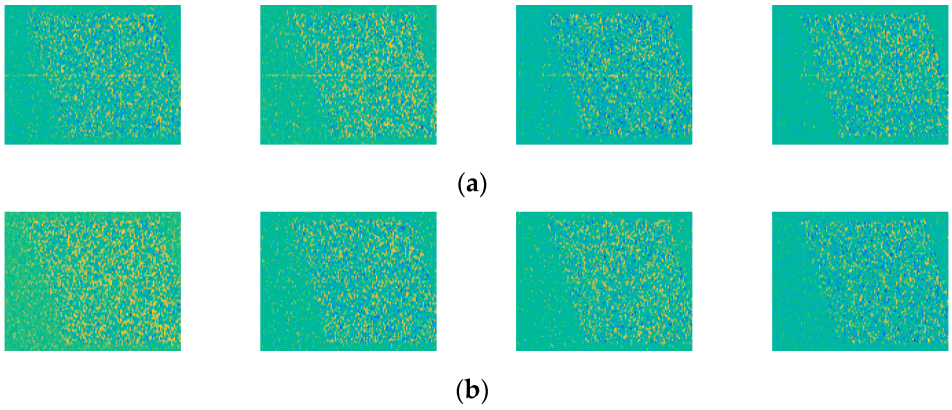

Figure 6. (**a**) Real part and (**b**) imaginary part of measured WBI-free SAR echoes in the time–frequency domain for training and testing the WBIM-GAN.

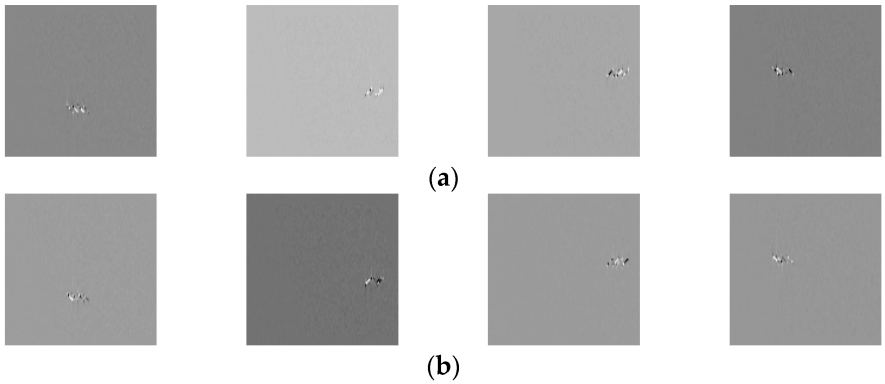

Figure 7. (**a**) Real part and (**b**) imaginary part of simulated SAR echoes with WBI corruption in the time–frequency domain for training and testing the WBIM-GAN.

3.2. Results of the Simulated Sentinel-1A Data with WBI Corruption

Figure 8 depicts the WBI mitigation results of WBIM-GAN performed on the validation set. It is obvious that the WBIM-GAN can effectively mitigate WBI. Figure 9 shows the training loss curves of IMN and WBIM-GAN with training iterations. It is evident that WBIM-GAN exhibits superior interference mitigation capabilities compared to IMN. To further confirm the efficiency of WBIM-GAN, we analyze the performance of different WBI mitigation algorithms under different jam-to-signal ratios (JSRs). Comparative WBI mitigation algorithms include GoDec, instantaneous-spectrum notch filtering (ISNF), Eigenspace projection (ESP), the iterative adaptive approach (IAA), matrix factorization decomposition (MFD), IMN, and WBIM-GAN. Figure 10 depicts the SDR curves of the seven above WBI mitigation methods when the JSR is set to 35 dB, 40 dB, 45 dB, 50 dB, and 55 dB. As can be seen, the data-driven WBI mitigation methods have a better performance. Meanwhile, the WBIM-GAN exhibits a superior performance in regard to mitigating WBI, and it should be emphasized that the SAR echoes recovered using the suggested approach have the lowest SDR compared to all the aforementioned methods for WBI mitigation. To further demonstrate the effectiveness of WBIM-GAN, we analyze the time–frequency distribution by using different WBI mitigation methods when the JSR is set to 50 dB, and the WBI mitigation results are represented in Figure 11. It is evident that the model-driven WBI mitigation methods can effectively mitigate WBI, but they cause significant distortion of the target signal. However, the IMN and WBIM-GAN can mitigate WBI and recover the target signal effectively. Simultaneously, the compared SDR and the WBI mitigation results demonstrate that the performance of WBIM-GAN is the best. Moreover, Figure 12 shows the class activation maps of the IMN and WBIM-GAN. It can be seen that IMN and WBIM-GAN focus on the region where WBI occurs, but the localized discriminative region

of WBIM-GAN is more concentrated, thus demonstrating that WBI-GAN outperforms IMN in terms of performance.

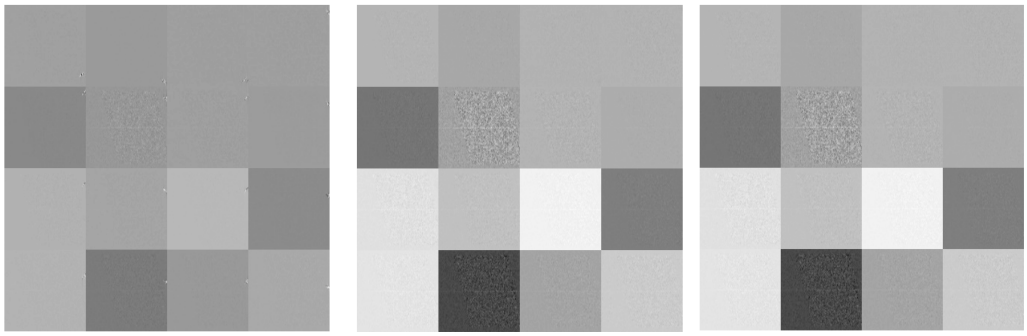

Figure 8. Comparisons with the original WBI-free SAR echoes, and the recovered SAR echoes after WBIM-GAN in TFD. (**a**) WBI-corrupted SAR echoes. (**b**) The original WBI-free SAR echoes. (**c**) The recovered SAR echoes after WBIM-GAN.

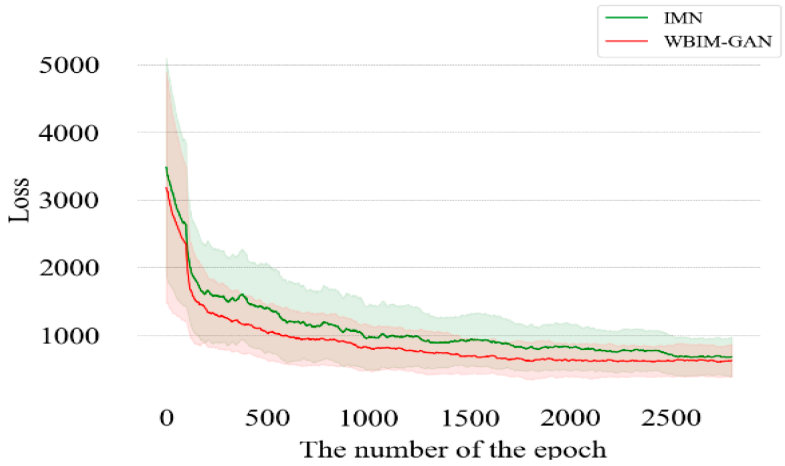

Figure 9. Comparison of the training loss with training iterations.

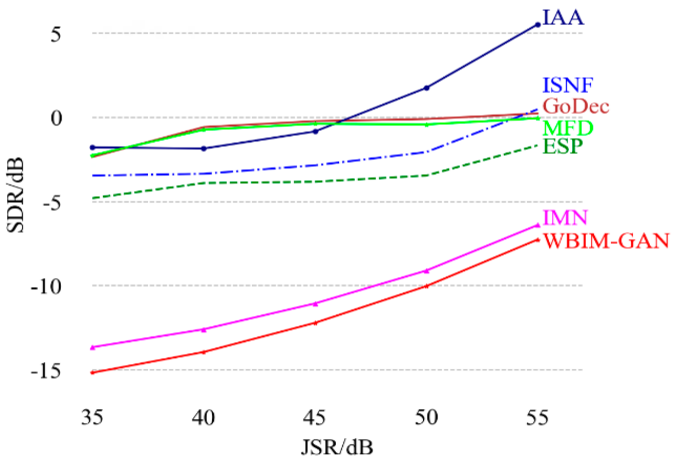

Figure 10. The SDR curves of different WBI mitigation methods.

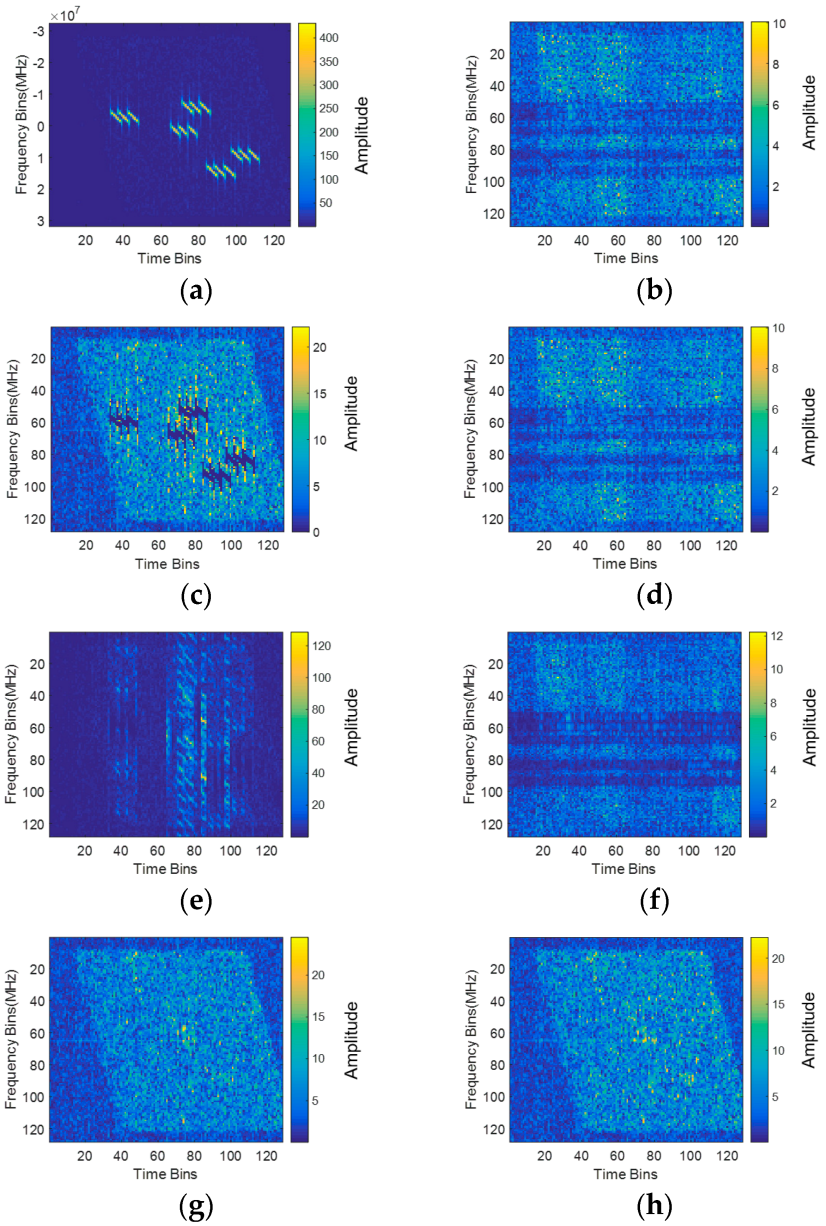

Figure 11. Comparison of mitigation results. (**a**) WBI-contaminated SAR echo. (**b**–**h**) WBI mitigation results after applying the GoDec, ISNF, ESP, IAA, MFD, IMN, and WBIM-GAN, respectively.

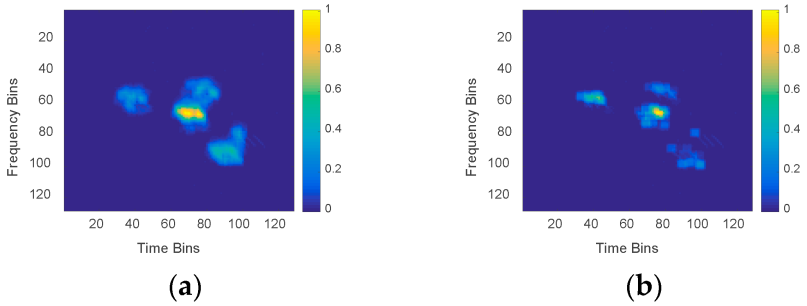

Figure 12. The class activation maps of the (**a**) IMN and (**b**) WBIM-GAN.

3.3. Results of the Measured WBI-Corrupted Sentinel-1A Data

In this part, we utilize Sentinel-1-collected WBI-corrupted SAR data in interferometric wide swath (IW) mode to validate the efficacy of the suggested WBI mitigation method.

Figure 13 shows the pseudo-color image of the real measured SAR data, and the parameters of the Sentinel-1 can be found in Table 4. To mitigate the WBI, the kurtosis of SAR echoes in the TFD is utilized to detect the WBI. Figure 14a shows the kurtosis of each SAR echo in the TFD before WBI mitigation. The red dotted line depicted in Figure 14a is the WBI detection threshold, and it is set to 9.3967 according to Equation (7). Figure 14b depicts the enlarged kurtosis. It is obvious that the kurtosis of the SAR echoes corrupted with WBI is relatively high. Figure 15 shows the 624th, 674th, and 1010th SAR echoes and the corresponding kurtosis. The 1010th SAR echo in the time–frequency domain is corrupted with strong WBI, and the corresponding kurtosis is much larger than the WBI detection threshold. Meanwhile, the 624th SAR echo is corrupted with weak WBI, and the corresponding kurtosis is also larger than the WBI detection threshold. Meanwhile, the kurtosis of the 674th WBI-free is smaller than the detection threshold. It can be seen that the kurtosis values of the 624th and 674th SAR echoes are very close to each other, but it can still accurately detect whether there is WBI in the SAR echo. The SAR echo shown in Figure 15c is corrupted with complex WBI, which is composed of multiple chirp-modulated WBIs, and the amplitude of WBI changes sharply. The presence of the nonstationary characteristic is apparent, as its magnitude fluctuates significantly over azimuth time, which puts forward higher requirements for the WBI detection and mitigation algorithm. Figure 16 shows the SAR image results corresponding to the area marked with a red rectangle in Figure 13. It is observed that the SAR image on the right is severely corrupted with WBI, which appears as haze-like artifacts. Meanwhile, targets under WBI coverage cannot be distinguished, which greatly impacts the precision of SAR image interpretation.

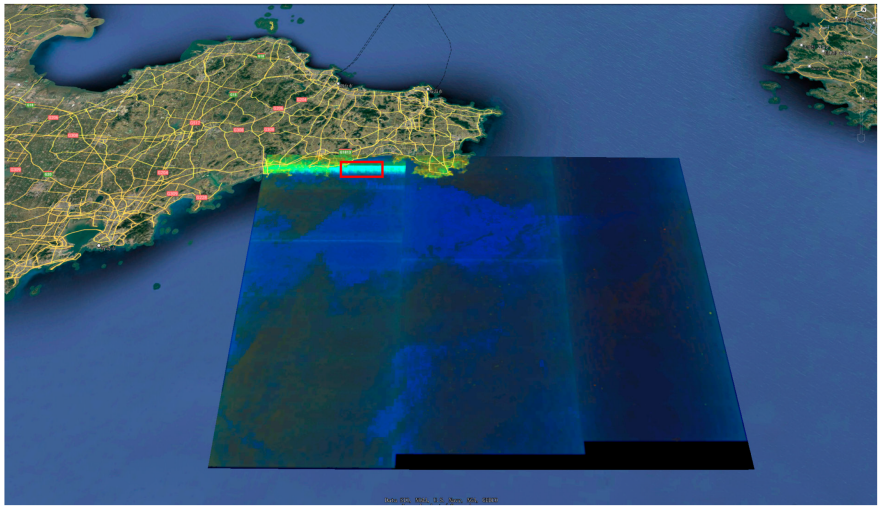

Figure 13. SAR image acquired by the European Sentinel-1A system.

Table 4. Parameters of the Sentinel-1A system.

Parameter	Value
Carrier frequency	5.405 GHz
Bandwidth	56.59 MHz
Sampling frequency	64.345 MHz
Pulse repetition frequency (PRF)	1717 Hz

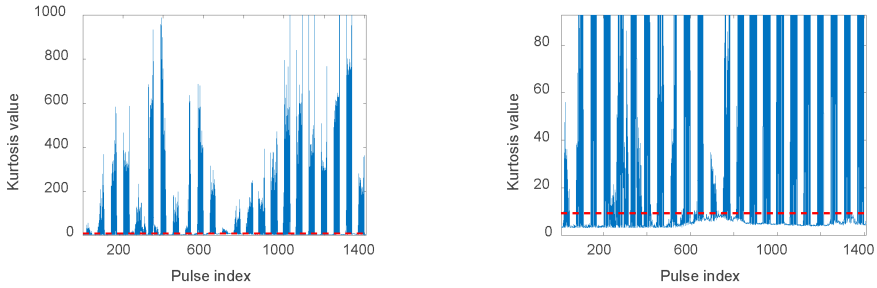

(**a**) (**b**)

Figure 14. (**a**) The WBI detection results at a false alarm rate of 10^{-3}. (**b**) The enlarged detection results in which the red dotted line is the WBI detection threshold and it is set to 9.3967.

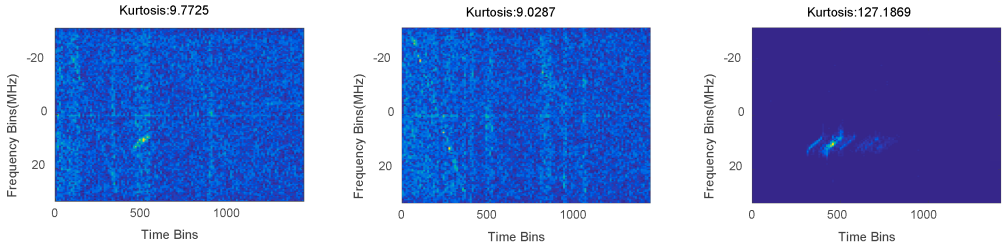

(**a**) (**b**) (**c**)

Figure 15. The representation of (**a**) 624th, (**b**) 674th, (**c**) and 1010th measured WBI-contaminated echoes with kurtosis value in the time–frequency domain.

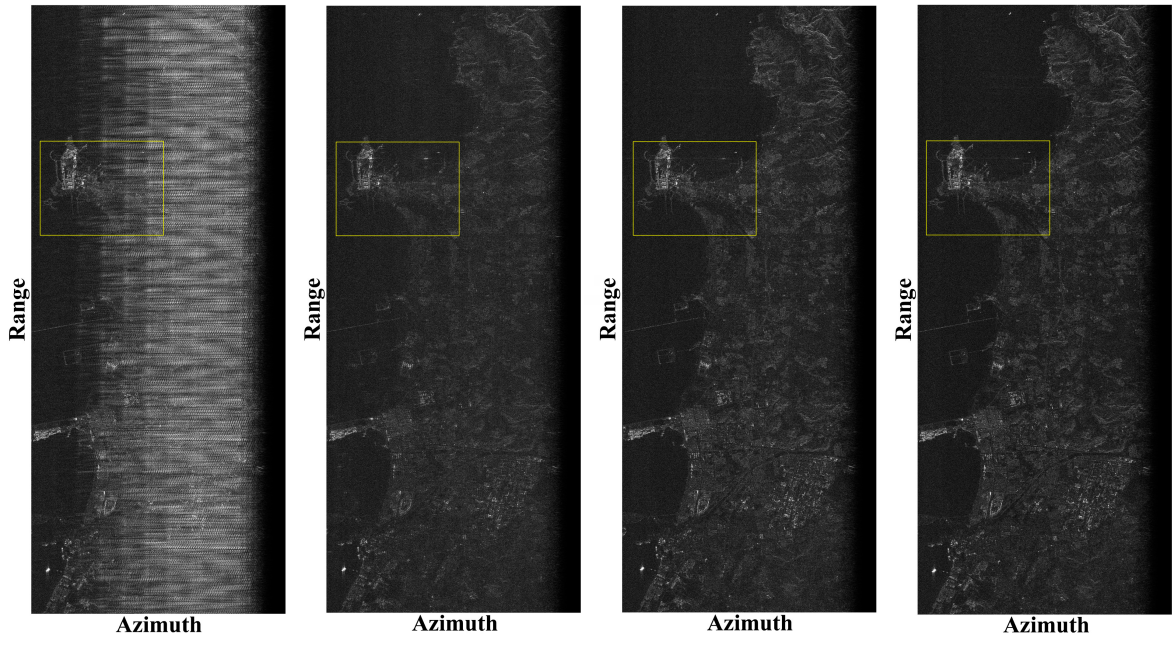

(**a**) (**b**) (**c**) (**d**)

Figure 16. *Cont.*

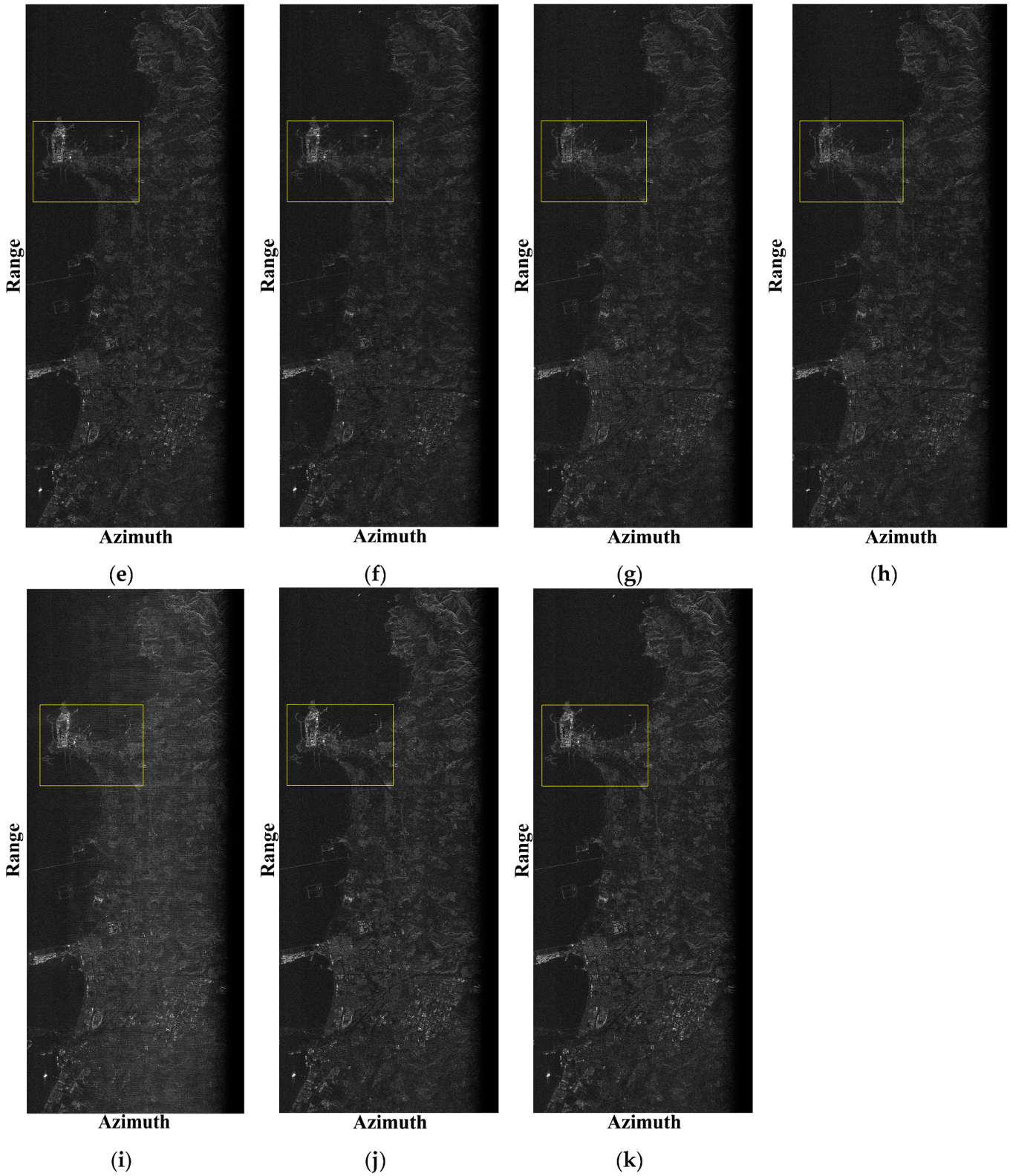

Figure 16. SAR imaging results (**a**) without WBI mitigation and after applying (**b**) GoDec, (**c**) ISNF, (**d**) ESP, (**e**) IAA, (**f**) MFD, (**g**) IMFD, (**h**) APMFD, (**i**) RPCA-TFP-JDA, (**j**) IMN, and (**k**) WBIM-GAN.

To illustrate the effectiveness of the WBIM-GAN, we compared and analyzed the WBI mitigation performance of GoDec, ISNF, ESP, IAA, MFD, IMFD, APMFD, and IMN. Figure 16b–k depicts the SAR imaging results with the implementation of GoDec, ISNF, ESP, IAA, MFD, IMFD, APMFD, RPCA-TFP-JDA [36], IMN, and WBIM-GAN, respectively.

Figure 17 is the magnified image and represents the detail of recovered target signals. From Figure 17b–f, it can be seen that the GoDec, ISNF, ESP, IAA, and MFD can effectively mitigate most of the WBI. However, these methods cause useful target echo loss, which results in defocusing and producing a false target, which is marked with the dotted green ellipse. Figure 17g,h shows the SAR imaging results utilizing the IMFD and APMFD in the SAR image domain. It is obvious that there is no false target, but the area marked with the dotted green ellipse has severe signal distortion. Figure 17i presents the SAR imaging results after applying the RPCA-TFP-JDA. It can be seen that most of the WBI is mitigated, and the targets contaminated by WBI are recovered. However, some WBIs marked with the dotted green ellipse still remain in the SAR imaging result. Figure 17j,k show the SAR imaging results by utilizing the IMN and WBIM-GAN. It is evident that the target is well focused. Table 5 shows the results of the MNR, SSIM, PSNR, and RMSE after applying different WBI mitigation algorithms. It should be noted that the pixels in blue are a no-return region, and the pixels in the red rectangle are the highlighted region in Figure 17a and are chosen for the computation of MNR. The WBI-free SAR image used to calculate SSIM, PSNR, and RMSE is shown in Figure 17l and was recorded by Sentinel-1A on 3 December 2020. It should be noted that the revisit cycle of Sentinel-1 is 6 days, so the acquired WBI-free SAR data from adjacent revisit cycles in the same region can be used for SSIM, PSNR, and RMSE. It is observed that the image obtained through the implementation of the suggested technique exhibits the most favorable response and image contrast among all of the above methods. Meanwhile, the suggested method exhibits a superior MNR, SSIM, PSNR, and RMSE performance. Moreover, due to the WBIM-GAN adopting the PatchGAN structure, the recovered target is more refined, and its performance is improved compared with IMN.

Table 5. Performance comparison.

Algorithms	MNR (dB)	SSIM	PSNR	RMSE
GoDec	−6.8082	0.8071	36.0737	0.4667
ISNF	−9.6385	0.8471	36.7555	0.3791
ESP	−10.4361	0.8597	36.9835	0.3757
IAA	−9.4438	0.8517	36.9612	0.3806
MFD	−7.5597	0.8441	36.7016	0.3940
IMFD	−7.8758	0.4064	28.2478	2.2445
APMFD	−8.1527	0.4981	29.8941	1.7547
RPCA-TFP-JDA	−9.8652	0.8195	36.1798	0.4336
IMN	−12.0819	0.8726	37.2718	0.3716
WBIM-GAN	−12.3211	0.8735	37.2894	0.3716

In addition, Table 6 shows the running time of the different WBI mitigation methods. All methods were tested on a workstation with an i7-6700K CPU and 64 GB memory. It is obvious that the ISNF can quickly mitigate the WBI by simply eliminating the prominent time–frequency bins. The GoDec and MFD algorithms demonstrate notable efficiency by applying the matrix factorization approach to accelerate the convergence process. To improve the performance of IAA, each SAR echo is divided into a lot of data with a length of 32 points for processing. Therefore, the running time of IAA is the longest. Meanwhile, the size of the SAR imaging result is 16,256 × 5000. To obtain the best WBI mitigation performance of the IMFD and APMFD, the SAR imaging result is divided into many 2000 × 2500 image blocks. Thus, the running time of IMFD and APMFD is longer than that of MFD. Meanwhile, the running time of RPCA-TFP-JDA is also longer than that of other WBI mitigation methods. The WBIM-GAN and IMN are performed on GPU, which reduces the computational burden. However, WBIM-GAN and IMN are designed in the TFD. Thus, much time is spent on STFT and ISTFT approaches.

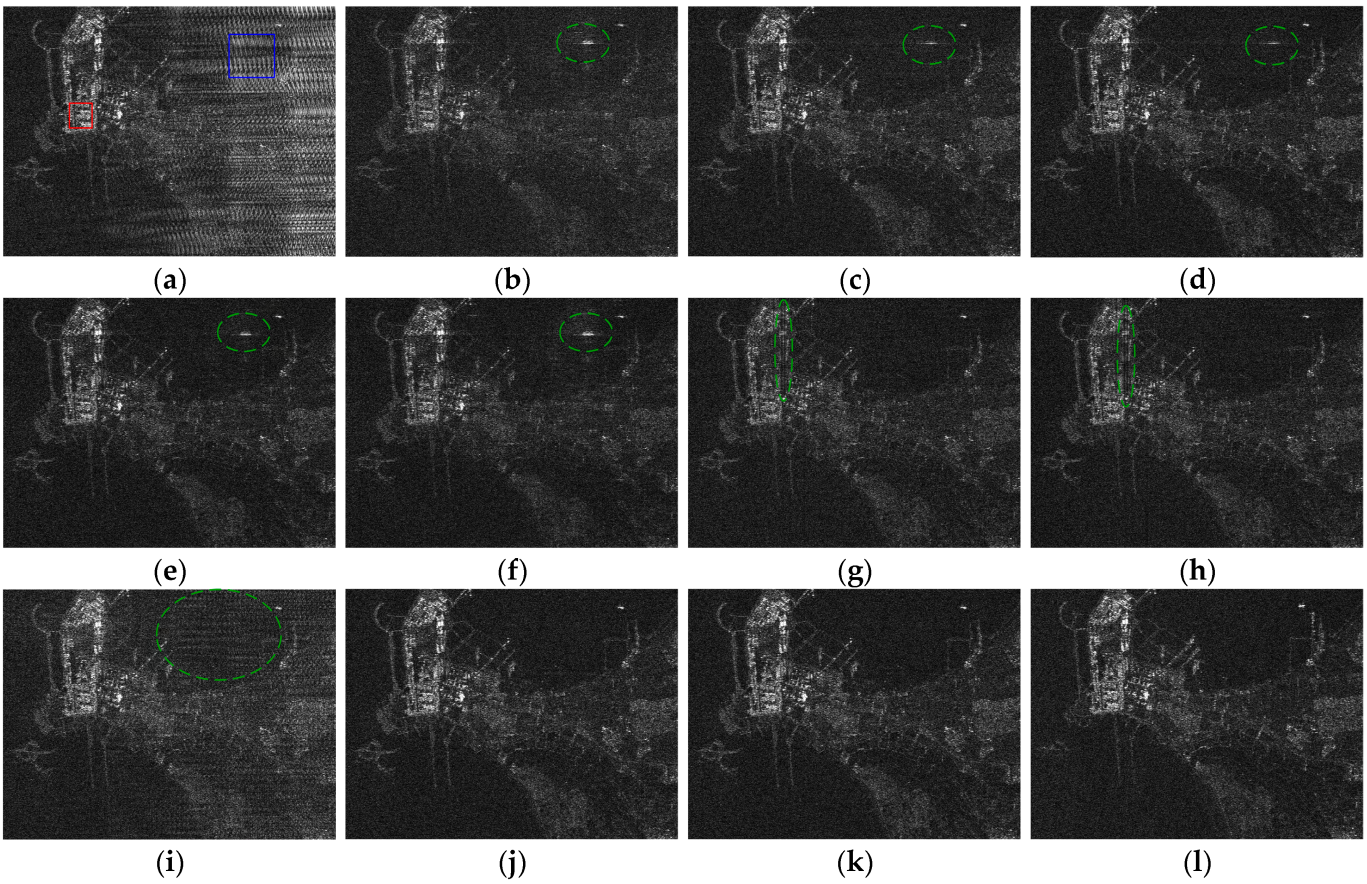

Figure 17. Enlarged SAR imaging results (**a**) without WBI mitigation and after applying (**b**) GoDec, (**c**) ISNF, (**d**) ESP, (**e**) IAA, (**f**) MFD, (**g**) IMFD, (**h**) APMFD, (**i**) RPCA-TFP-JDA, (**j**) IMN, and (**k**) WBIM-GAN. (**l**) WBI-free SAR image acquired in the same area.

Table 6. Running times of different WBI mitigation methods.

Algorithms	Running Time (s)
GoDec	21.713
ISNF	21.703
ESP	68.510
IAA	3011.68
MFD	25.78
IMFD	40.98
APMFD	109.18
RPCA-TFP-JDA	235.883
IMN	26.587
WBIM-GAN	32.691

3.4. Results of the Measured WBI-Corrupted Sentinel-1B Data

To validate the efficiency of the WBIM-GAN further, the effectiveness of various methods is compared and analyzed to mitigate WBI on the recorded data obtained from Sentinel-1B near Seoul, South Korea, on 28 December 2020. The radar system parameters of Sentinel-1B are the same as those of Sentinel-1A. Figure 18 displays the pseudo-color representation of the recorded data.

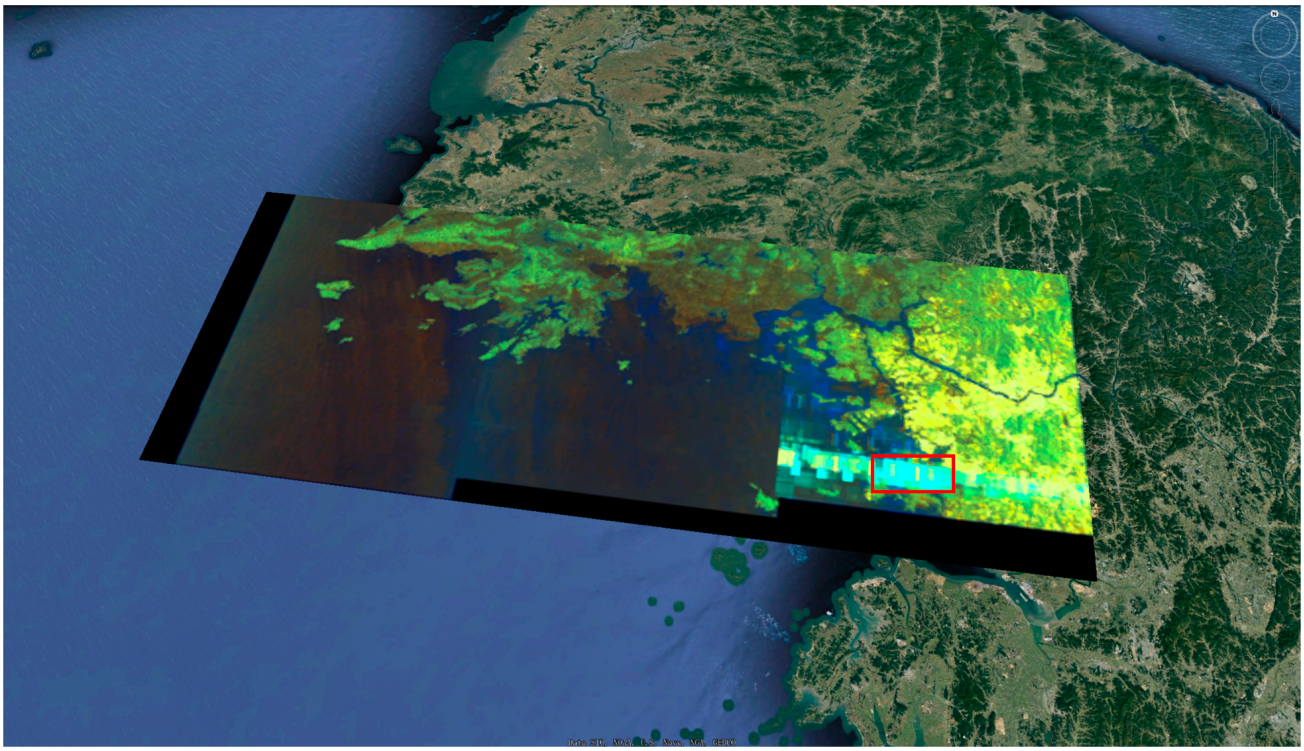

Figure 18. The SAR image was acquired by the European Sentinel-1B system.

Furthermore, the SAR imaging results of implementing the GoDec, ISNF, ESP, IAA, MFD, IMFD, APMFD, RPCA-TFP-JDA, IMN, and WBIM-GAN are illustrated in Figure 19, which corresponds to the region indicated by a red rectangle in Figure 18. The SAR image is heavily distorted by WBI in the central portion, making it nearly impossible to extract any meaningful information. Figure 20 represents the magnified SAR images of the region, highlighted by a yellow rectangle in Figure 19. It is obvious that all techniques for mitigating WBI are effective and make the city clearly visible. However, the GoDec, IAA, and MFD cause fewer signal losses and distortion, which is marked with a green dot ellipse. Meanwhile, the ISNF, ESP, and RPCA-TFP-JDA cause less WBI to be left in the SAR images marked with the green dot ellipse. Moreover, the IMFD and APMFD introduce much signal loss marked with a green dot ellipse. It is evident that both the WBIM-GAN and IMN demonstrate comparable performances, with the SAR imaging outcomes being of high quality. The comparison results of the MNR, SSIM, PSNR, and RMSE for the SAR imaging results depicted in Figure 20 are presented in Table 7. Similarly, the pixels in the blue are the no-return region, and the pixels in the red rectangle in the highlighted region in Figure 20a were chosen for calculating the MNR. Meanwhile, the WBI-free SAR image used to calculate SSIM, PSNR, and RMSE is shown in Figure 20l. According to Table 7, the WBIM-GAN approach demonstrates a lower MNR and RMSE value, as well as a larger SSIM and PSNR value, illustrating a refined recovery of the system image output and heightened image contrast. The running times of different WBI mitigation methods are listed in Table 8. It is obvious that the proposed WBIM-GAN exhibits a superior WBI mitigation performance, along with a relatively faster running speed.

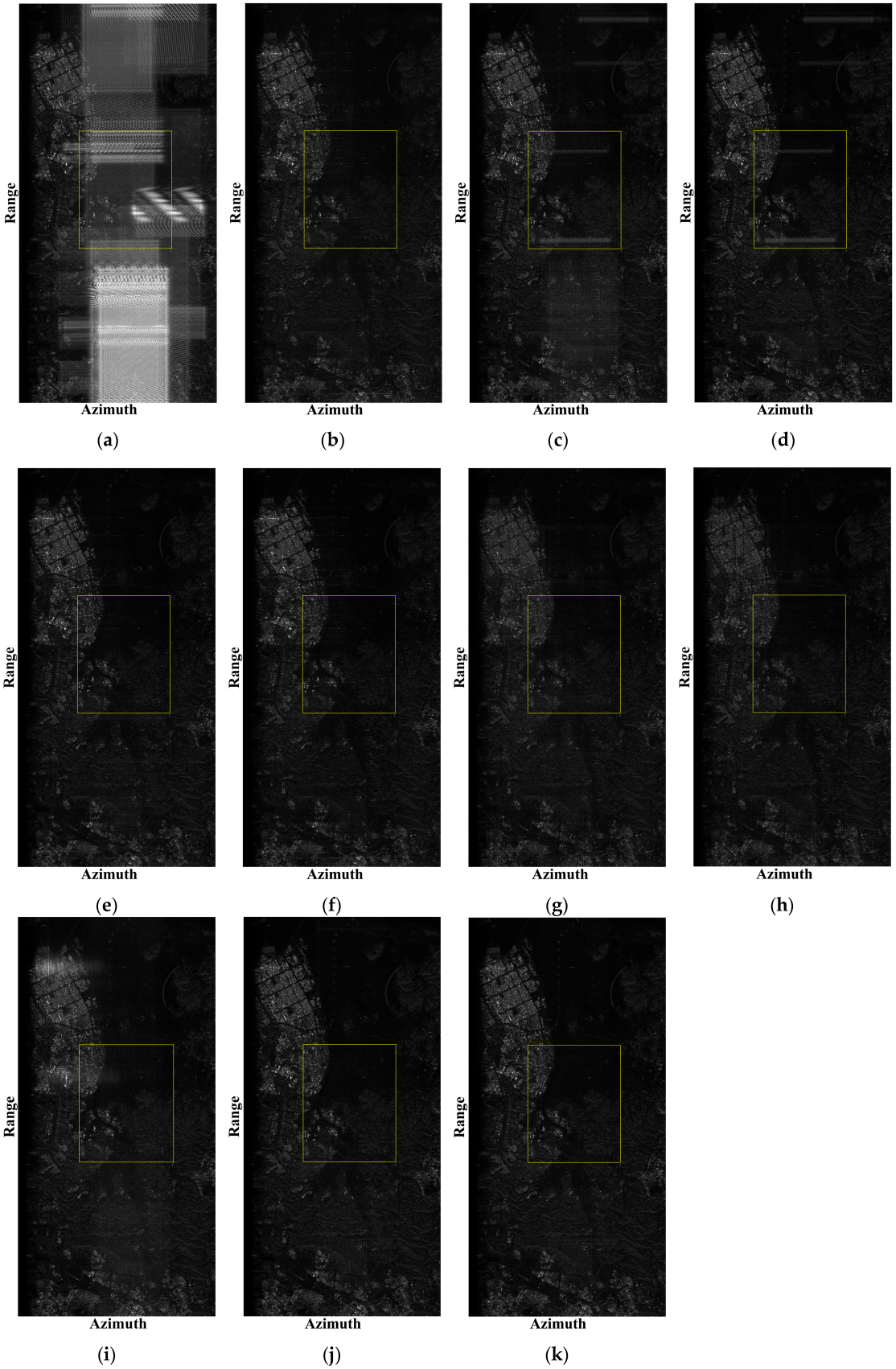

Figure 19. SAR imaging results (**a**) without WBI mitigation and after applying (**b**) GoDec, (**c**) ISNF, (**d**) ESP, (**e**) IAA, (**f**) MFD, (**g**) IMFD, (**h**) APMFD, (**i**) RPCA-TFP-JDA, (**j**) IMN, and (**k**) WBIM-GAN.

Table 7. Performance comparison.

Algorithms	MNR (dB)	SSIM	PSNR	RMSE
GoDec	−7.4943	0.7768	35.3005	0.6800
Tffilter	−7.1579	0.8011	35.5124	0.6465
Eigfilter	−8.2282	0.8332	35.8156	0.5366
IAA	−9.2969	0.8251	35.7949	0.4975
MFD	−8.8208	0.8191	35.6881	0.5358
IMFD	−8.8428	0.6623	33.4477	1.1715
APMFD	−8.4524	0.6146	32.4047	1.4018
RPCA-TFP-JDA	−8.6186	0.7982	35.4474	0.6057
IMN	−10.5136	0.8454	35.9998	0.4051
WBIM-GAN	−10.8336	0.8482	36.0106	0.3939

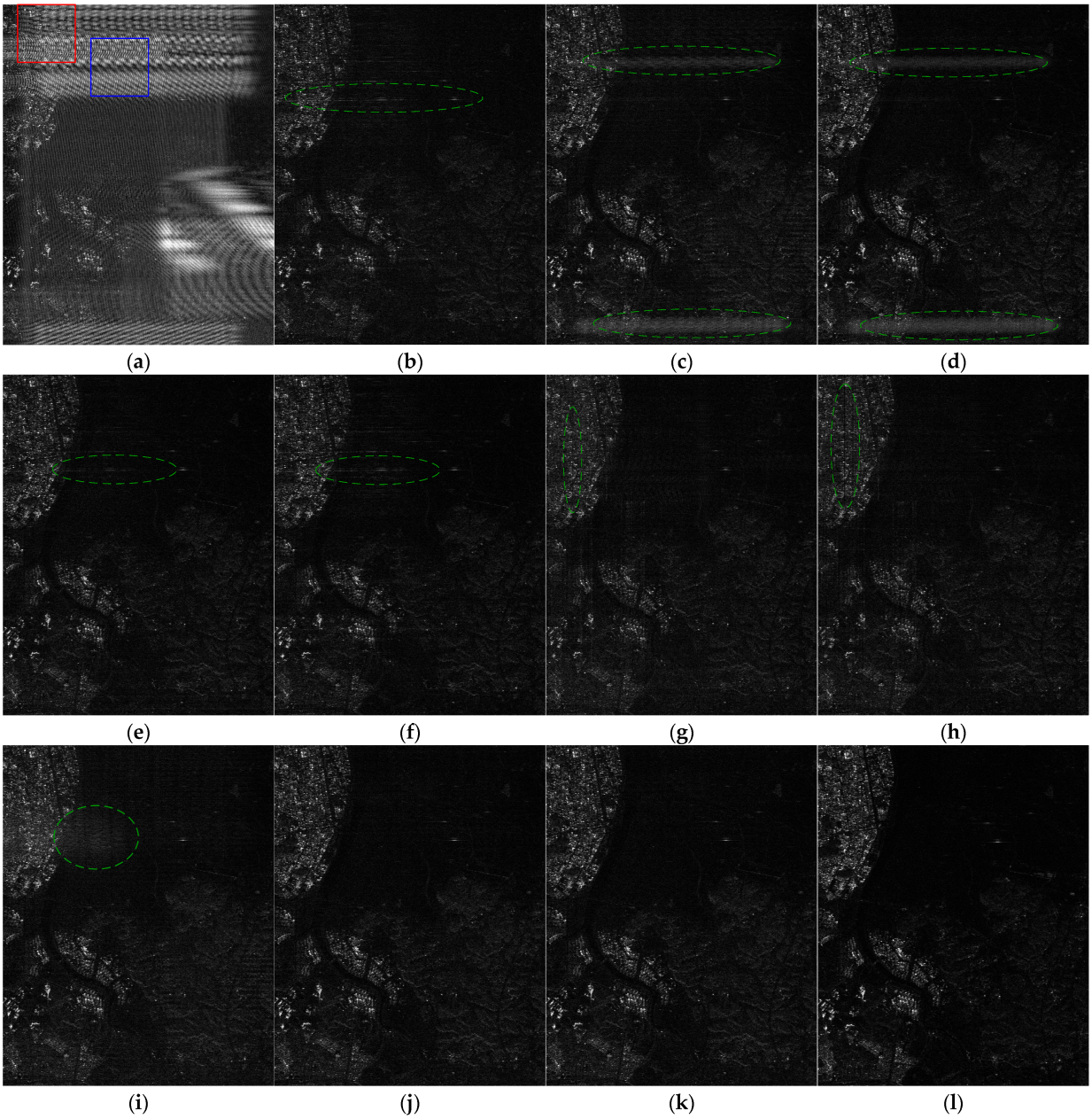

Figure 20. Enlarged SAR imaging results (**a**) without WBI mitigation and after applying (**b**) GoDec, (**c**) ISNF, (**d**) ESP, (**e**) IAA, (**f**) MFD, (**g**) IMFD, (**h**) APMFD, (**i**) RPCA-TFP-JDA, (**j**) IMN, and (**k**) WBIM-GAN. (**l**) WBI-free SAR image acquired in the same area.

Table 8. Running times of different WBI mitigation methods.

Algorithms	Running Time (s)
GoDec	11.772
ISNR	11.721
ESP	35.930
IAA	1379.250
MFD	12.400
IMFD	35.440
APMFD	143.230
RPCA-TFP-JDA	228.101
IMN	15.938
WBIM-GAN	15.626

4. Discussion

This paper proposes a WBI mitigation algorithm based on GAN (WBI-GAN). Compared with previous WBI mitigation algorithms, Such as GoDec, ISNF, ESP, IAA, MFD, IMFD, and APMFD, the WBI-GAN mapped from an input WBI-corrupted echo to its properly WBI-free echo in an end-to-end data-driven approach. It is composed of a WBI mitigation network and a target echo discriminative network. The WBI mitigation network utilizes a deep residual network to solve the issue of gradient saturation and further boost the performance of WBI mitigation. The target echo discriminative network adopts the PatchGAN architecture to improve the WBI mitigation's effectiveness by capturing the local texture and statistical features of target echoes. The WBI mitigation results of GoDec, ISNF, ESP, IAA, MFD, IMFD, APMFD, IMN, and WBI-GAN on one simulated and two measured SAR data verify the WBI mitigation performance of the WBI-GAN. Moreover, the comparison results of the MNR, SSIM, PSNR, and RMSE in Section 3 further prove the effectiveness and priority of the WBI-GAN.

Most WBI mitigation methods are model-driven approaches, which mainly utilize physical and prior knowledge to construct parameterized and non-parameterized WBI mitigation models and then achieve effective WBI mitigation. However, those methods severely depend on high model accuracy, which would otherwise result in target echo loss. The WBIM-GAN is a new WBI mitigation method that can achieve useful target signal accuracy reconstruction without any prior knowledge of WBI and target echo. Moreover, it simplifies the difficulty of designing a WBI mitigation algorithm in an end-to-end data-driven way.

The WBI-GAN can effectively mitigate the chirp-modulated and sinusoidal-modulated WBI for SAR. However, the mitigation performance may be degraded for some complex forms of WBI, which cannot be expressed by the equation shown in Section 2.1. In the future, we will include more forms of WBI to improve the performance of the proposed framework.

5. Conclusions

In this paper, we propose a novel data-driven method for mitigating WBI, which is implemented by using a generative adversarial network. By considering the differences in structural features between WBI and the target signal in the TFD, this method employs GAN and PatchGAN architecture to capture the improved characteristics of the target signal and then restore it. Meanwhile, several real SAR data corrupted with WBI acquired from the Sentinel-1 satellite are utilized to evaluate the efficacy of the WBIM-GAN. Furthermore, in order to compare the alleviation effects of different WBI mitigation methods, various quantitative metrics, such as MNR, SSIM, PSNR, and RMSE, are utilized to implement the comparison. And the final results verify the advantages of the WBIM-GAN. However, the mitigation performance of the WBI-GAN may be degraded in some situations in which complex forms of WBI cannot be expressed by the WBI samples contained in the training dataset. Therefore, we would include more forms of complex WBI in the training dataset to improve the WBI mitigation performance of the WBI-GAN in the future.

Author Contributions: Conceptualization, X.X.; methodology, X.X.; validation, S.W.; investigation, S.W.; resources, W.F.; data curation, W.F.; writing—original draft, X.X.; writing—review and editing, W.F.; funding acquisition, F.Z. All authors have read and agreed to the published version of the manuscript.

Funding: This work was funded in part by the National Natural Science Foundation of China, under Grant Nos. 62001350, 62101412, and 62101418; and by the China Postdoctoral Science Foundation, under Grant 2020M673346.

Data Availability Statement: Data are contained within the article.

Conflicts of Interest: The authors declare no conflict of interest.

References

1. Moreira, A.; Prats-Iraola, P.; Younis, M.; Krieger, G.; Hajnsek, I.; Papathanassiou, K.P. A tutorial on synthetic aperture radar. *IEEE Geosci. Remote Sens.* **2013**, *1*, 6–43. [CrossRef]
2. Reigber, A.; Scheiber, R.; Jager, M.; Pau, P.L.; Hajnsek, I.; Jagdhuber, T. Very-high-resolution airborne synthetic aperture radar imaging: Signal processing and applications. *Proc. IEEE* **2013**, *101*, 759–783. [CrossRef]
3. Ghaderpour, E.; Antonielli, B.; Bozzano, F.; Mugnozza, G.; Mazzanti, P. A fast and robust method for detecting trend turning points in InSAR displacement time series. *Comput. Geosci.* **2023**, *185*, 105546. [CrossRef]
4. Shi, W.; Hu, Z.; Liu, H.; Cen, S.; Huang, J.; Chen, X. Ship Detection in SAR Images Based on Adjacent Context Guide Fusion Module and Dense Weighted Skip Connection. *IEEE Access* **2022**, *10*, 134263–134276. [CrossRef]
5. Tao, M.; Lai, S.; Li, J.; Su, J.; Fan, Y.; Wang, L. Extraction and mitigation of radio frequency interference artifacts based on time-series sentinel-1 sar data. *IEEE Trans. Geosci. Remote Sens.* **2021**, *60*, 5217211. [CrossRef]
6. Lv, Z.; Fan, H.; Chen, Z.; Qiu, J.; Ren, M.; Zhang, Z. Mitigate the LFM-PRFI in SAR data: Joint down-range and cross-range filtering. *IEEE Trans. Geosci. Remote Sens.* **2023**, *61*, 5205918. [CrossRef]
7. Su, J.; Tao, H.; Tao, M.; Wang, L.; Xie, J. Narrowband interference suppression via RPCA-based signal separation in time–frequency domain. *IEEE J. Sel. Topics Appl. Earth Observ. Remote Sens.* **2017**, *10*, 5016–5025. [CrossRef]
8. Zhou, F.; Xing, M.; Bai, X.; Sun, G.; Bao, Z. Narrowband interference suppression for SAR based on complex empirical mode decomposition. *IEEE Trans. Geosci. Remote Sens.* **2012**, *50*, 3202–3218.
9. Vehmas, R.; Radius, A.; Dogan, O.; Ignatenko, V.; Leprovost, P.; Lamentowski, L.; Muff, D.; Nottingham, M.; Seilonen, T.; Vilja, P. Mitigation of RFI in high-resolution SAR data-algorithm overview and experimental demonstration. In Proceedings of the International Radar Symposium, Berlin, Germany, 24–26 May 2023; pp. 1–9.
10. Ojowu, O., Jr.; Li, J. RFI suppression for synchronous impulse reconstruction UWB radar using RELAX. *Int. J. Remote Sens. Appl.* **2013**, *3*, 33–46.
11. Ding, Y.; Fan, W.; Tao, M.; Zhang, Z.; Wang, L.; Zhou, F. Wideband interference mitigation for synthetic aperture radar based on the variational Bayesian method. *Signal Process* **2022**, *198*, 108581. [CrossRef]
12. Huang, Y.; Zhang, L.; Li, J.; Chen, Z.; Yang, X. Reweighted tensor factorization method for SAR narrowband and wideband interference mitigation using smoothing multiview tensor model. *IEEE Trans. Geosci. Remote Sens.* **2020**, *58*, 3298–3313. [CrossRef]
13. Huang, Y.; Zhang, L.; Li, J.; Hong, W.; Nehorai, A. A Novel Tensor Technique for Simultaneous Narrowband and Wideband Interference Suppression on Single-Channel SAR System. *IEEE Trans. Geosci. Remote Sens.* **2019**, *57*, 9575–9588. [CrossRef]
14. Liu, H.; Li, D.; Zhou, Y.; Truong, T. Simultaneous radio frequency and wideband interference suppression in SAR signals via sparsity exploitation in time–frequency domain. *IEEE Trans. Geosci. Remote Sens.* **2018**, *56*, 5780–5793. [CrossRef]
15. Ding, Y.; Fan, W.; Zhang, Z.; Zhou, F.; Lu, B. Radio Frequency Interference Mitigation for Synthetic Aperture Radar Based on the Time-Frequency Constraint Joint Low-Rank and Sparsity Properties. *Remote Sens.* **2022**, *14*, 775. [CrossRef]
16. Huang, Y.; Liao, G.; Zhang, Z.; Xiang, Y.; Li, J.; Nehorai, A. Fast narrowband RFI suppression algorithms for SAR systems via matrix factorization techniques. *IEEE Trans. Geosci. Remote Sens.* **2019**, *57*, 250–262. [CrossRef]
17. Huang, Y.; Chen, Z.; Wen, C.; Xia, X.; Hong, W. An efficient radio frequency interference mitigation algorithm in real synthetic aperture radar data. *IEEE Trans. Geosci. Remote Sens.* **2022**, *60*, 1–12. [CrossRef]
18. Tao, M.; Zhou, F.; Zhang, Z. Wideband interference mitigation in high-resolution airborne synthetic aperture radar data. *IEEE Trans. Geosci. Remote Sens.* **2016**, *54*, 74–87. [CrossRef]
19. Yang, Z.; Du, W.; Liu, Z.; Liao, G. WBI suppression for SAR using iterative adaptive method. *IEEE J. Sel. Topics Appl. Earth Observ.* **2016**, *9*, 1008–1014. [CrossRef]
20. Krizhevsky, A.; Sutskever, I.; Hinton, G. ImageNet classification with deep convolutional neural networks. *Commun. ACM* **2012**, *60*, 84–90. [CrossRef]
21. Ren, S.; He, K.; Girshick, R.; Sun, J. Faster r-cnn: Towards real-time object detection with region proposal networks. *IEEE Trans. Pattern Anal. Mach. Intell.* **2015**, *39*, 1137–1149. [CrossRef]
22. Shelhamer, E.; Long, J.; Darrell, T. Fully convolutional networks for semantic segmentation. *IEEE Trans. Pattern Anal. Mach. Intell.* **2017**, *39*, 640–651. [CrossRef]

23. Michelsanti, D.; Tan, Z. Conditional generative adversarial networks for speech enhancement and noise-robust speaker verification. In Proceedings of the Annual Conference of the International Speech Communication Association 2008–2012, Stockholm, Sweden, 20–24 August 2017.
24. Ledig, C.; Theis, L.; Huszár, F.; Caballero, J.; Cunningham, A.; Acosta, A.; Aitken, A.; Tejani, A.; Totz, J.; Wang, Z.; et al. Photo-realistic single image super-resolution using a generative adversarial network. In Proceedings of the IEEE Conference on Computer Vision and Pattern Recognition 2017 (CVPR), Honolulu, HI, USA, 21–26 January 2017; pp. 105–114.
25. Goodfellow, I.J.; Pouget-Abadie, J.; Mirza, M.; Xu, B.; Warde-Farley, D.; Ozair, S.; Courville, A.; Bengio, Y. Generative adversarial networks. In Proceedings of the Advances in Neural Information Processing Systems (NIPS), Montreal, QC, Canada, 8–11 December 2014; pp. 2672–2680.
26. Arjovsky, M.; Chintala, S.; Bottou, L. Wasserstein generative adversarial networks. In Proceedings of the International Conference on Machine Learning (ICML), Sydney, Australia, 6–11 August 2017; pp. 298–321.
27. Gulrajani, I.; Ahmed, F.; Arjovsky, M.; Dumoulin, V.; Courville, A. Improved training of wasserstein GANs. In Proceedings of the Advances in Neural Information Processing Systems (NIPS), Long Beach, CA, USA, 4–9 December 2017; pp. 5768–5778.
28. Isola, P.; Zhu, J.-Y.; Zhou, T.; Efros, A.A. Image-to-image translation with conditional adversarial networks. In Proceedings of the IEEE Conference on Computer Vision and Pattern Recognition (CVPR), Honolulu, HI, USA, 21–26 July 2017; pp. 5967–5976.
29. Zhang, Z.; Ding, Y.; Fan, W.; Zhou, F.; Lu, B. Wideband interference mitigation for sar based on generative adversarial network. In Proceedings of the International Radar Conference, Haikou, China, 15–19 December 2021; pp. 1–4.
30. Tao, M.; Li, J.; Su, J.; Wang, L. Characterization and removal of rfi artifacts in radar data via model-constrained deep learning approach. *Remote Sens.* **2022**, *14*, 1578. [CrossRef]
31. Fan, W.; Zhou, F.; Tao, M.; Bai, X.; Rong, P.; Yang, S.; Tian, T. Interference mitigation for synthetic aperture radar based on deep residual network. *Remote Sens.* **2019**, *11*, 1654. [CrossRef]
32. Nair, A.; Rangamani, A.; Nguyen, L.; Bell, M.; Tran, T. Spectral gap extrapolation and radio frequency interference suppression using 1d unets. In Proceedings of the IEEE National Radar Conference, Atlanta, GA, USA, 7–14 May 2021; pp. 1–4.
33. Fuchs, A.; Rock, J.; Toch, M.; Meissner, R.; Pernkopf, F. Complex-valued convolutional neural networks for enhanced radar signal denoising and interference mitigation. In Proceedings of the IEEE National Radar Conference, Atlanta, GA, USA, 7–14 May 2021; pp. 1–4.
34. Meyer, F.J.; Nicoll, J.B.; Doulgeris, A.P. Correction and characterization of radio frequency interference signatures in l-band synthetic aperture radar data. *IEEE Trans. Geosci. Remote Sens.* **2013**, *51*, 4961–4972. [CrossRef]
35. Zhou, F.; Tao, M. Research on methods for narrowband interference suppression in synthetic aperture radar data. *IEEE J. Sel. Topics Appl. Earth Observ.* **2015**, *8*, 7. [CrossRef]
36. Su, J.; Xi, M.; Gong, Y.; Tao, M.; Fan, Y.; Wang, L. Time-Varying Wideband Interference Mitigation for SAR via Time-Frequency-Pulse Joint Decomposition Algorithm. *IEEE Trans. Geosci. Remote Sens.* **2022**, *60*, 5118816. [CrossRef]